

Article

Large Negative Photoresistivity in Amorphous NdNiO₃ Film

Alexandr Stupakov ^{1,*}, Tomas Kocourek ¹ , Natalia Nepomniashchaia ^{1,2}, Marina Tyunina ^{1,3} 
and Alexandr Dejneka ^{1,*} 

¹ Institute of Physics of the Czech Academy of Sciences, Na Slovance 2, 18221 Prague, Czech Republic; kocourek@fzu.cz (T.K.); nepomni@fzu.cz (N.N.); tjunina@fzu.cz (M.T.)

² Faculty of Nuclear Sciences and Physical Engineering, Czech Technical University in Prague, Technická 2, 16627 Prague, Czech Republic

³ Microelectronics Research Unit, Faculty of Information Technology and Electrical Engineering, University of Oulu, P.O. Box 4500, FI-90014 Oulu, Finland

* Correspondence: stupak@fzu.cz (A.S.); dejneka@fzu.cz (A.D.)

Abstract: A significant decrease in resistivity by 55% under blue lighting with $\sim 0.4 \text{ J} \cdot \text{mm}^{-2}$ energy density is demonstrated in amorphous film of metal-insulator NdNiO₃ at room temperature. This large negative photoresistivity contrasts with a small positive photoresistivity of 8% in epitaxial NdNiO₃ film under the same illumination conditions. The magnitude of the photoresistivity rises with the increasing power density or decreasing wavelength of light. By combining the analysis of the observed photoresistive effect with optical absorption and the resistivity of the films as a function of temperature, it is shown that photo-stimulated heating determines the photoresistivity in both types of films. Because amorphous films can be easily grown on a wide range of substrates, the demonstrated large photo(thermo)resistivity in such films is attractive for potential applications, e.g., thermal photodetectors and thermistors.

Keywords: rare-earth nickelates; epitaxial perovskite films; amorphous thin films; photoconductivity



Citation: Stupakov, A.; Kocourek, T.; Nepomniashchaia, N.; Tyunina, M.; Dejneka, A. Large Negative Photoresistivity in Amorphous NdNiO₃ Film. *Coatings* **2021**, *11*, 1411. <https://doi.org/10.3390/coatings11111411>

Academic Editor: Alessio Lamperti

Received: 17 October 2021

Accepted: 17 November 2021

Published: 19 November 2021

Publisher's Note: MDPI stays neutral with regard to jurisdictional claims in published maps and institutional affiliations.



Copyright: © 2021 by the authors. Licensee MDPI, Basel, Switzerland. This article is an open access article distributed under the terms and conditions of the Creative Commons Attribution (CC BY) license (<https://creativecommons.org/licenses/by/4.0/>).

1. Introduction

Rare-earth nickelates is a separate class of perovskite-structure metal oxides, whose main feature is specific resistive behavior. The end-member of the series LaNiO₃ (LNO) with a rhombohedral crystallographic structure exhibits the metallic conductivity at all temperatures. Low conductivity and superior catalytic properties make LNO attractive for use as functional sublayers in perovskite heterostructures [1]. Other nickelates with the orthorhombic structure display a sharp metal-to-insulator transition (MIT) from a high-temperature paramagnetic metal state to a low-temperature antiferromagnetic insulator. At MIT, the electrical resistivity changes by several orders of magnitude, which holds promise for many device applications. The most attractive members are NdNiO₃ (NNO) and SmNiO₃ (SNO), whose MIT temperatures $T_{MI} \approx 200$ and 400 K for bulk ceramics are the closest to room temperature [2,3].

Nowadays, a focus in the research has moved to the investigation of epitaxial thin films and heterostructures, which follow an in-plane structure of similar perovskite substrate. A film–substrate mismatch in the lattice parameters introduces a strain influencing the resistive behavior of the nickelate thin films as compared with their bulk analogues [4,5]. For instance, the most studied NNO films subjected to a tensile strain of $\sim 2\%$ have $T_{MI} \approx 170$ K, whereas a small compressive strain of $< -0.3\%$ fully suppresses MIT in these films [6–9]. Recently, T_{MI} at room temperature range is observed in SNO/NNO repetitive heterostructures with a few unit-cell thicknesses of separate layers [10]. However, the epitaxial growth is restricted by the selection of appropriate expensive substrates.

A hot trend of modern research is to extend the films functionality by an external physical stimulus. One of the attractive possibilities is to stimulate MIT in nickelates by irradiation with light [11]. However, the first attempts to switch MIT optically surmise

the dominating influence of local sample heating due to light absorption [10,12]. Another promising direction of modern research is to study the polycrystalline perovskite films, which can be deposited on cheap industrial substrates [1,13–16].

We pursued two main objectives in this work. First, we comprehensively studied the photoresistivity at room temperature in epitaxial nickelate films to clarify a physical origin of the effect. Second, we demonstrated a strong photoresistive response in a novel material: amorphous film of NNO. Whereas a small resistivity increase of a few percent was observed in the epitaxial NNO films, a large drop of resistivity under irradiation was obtained for the amorphous film of the same elemental composition. We believe that this finding can stimulate broader research of non-epitaxial (oriented, polycrystalline and amorphous) nickelate films, which are currently practically unexplored [13,14,17].

2. Materials and Methods

Thin nickelate films were grown by pulsed laser deposition using a KrF excimer laser of $2\text{ J}\cdot\text{cm}^{-2}$ energy density and ambient oxygen pressure of 20 Pa. The substrates purchased from the MTI Corporation (Richmond, VA, USA) were kept at temperature of 700 °C during the deposition [9]. In the main part of this paper, we confront the photoresistive response in two NNO films of 80 nm thickness: one film on (001)($\text{La}_{0.3}\text{Sr}_{0.7}$)($\text{Al}_{0.65}\text{Ta}_{0.35}$) O_3 (LSAT) and another film on SiO_2 (quartz) substrates. These films were deposited simultaneously within the same process, which ensured their identical elemental composition. Supporting data for other epitaxial films (LNO, NNO and SNO) of different thicknesses 20–120 nm deposited on LSAT or (001) LaAlO_3 (LAO) substrates are shown in Appendix A.

X-ray diffraction patterns were recorded by a multipurpose intelligent Empyrean diffractometer of 3rd generation (Malvern Panalytical Ltd., Malvern, UK) using $\text{Cu-K}\alpha$ radiation with a wavelength 1.540598 Å. Two main films shown in Figure 1 were investigated in the grazing incidence geometry in a 2θ range from 0 to 90°. The epitaxial NNO film on LSAT substrate was also measured using the Bragg–Brentano geometry in a 2θ range from 10 to 120°. For accurate peak separation, the bare LSAT substrate was additionally investigated in the Bragg–Brentano geometry. The data were analyzed using Match! software (version 2.4.7, Crystal Impact, Bonn, Germany).

For electrical characterization, four stripe-type golden contacts of 1 mm width separated by 2 mm each were deposited on the top of the films ($10 \times 10\text{ mm}^2$ size) by pulsed laser deposition at 200 °C through a shadow mask. Then the samples were cut into three identical pieces of $3.2 \times 10\text{ mm}^2$ size (photo of the samples is shown in Figure 1e). DC resistance was measured by a digital multimeter DMM6500 (Keithley Instruments, Cleveland, OH, USA) through USB remote interface. A precise 4-wire method was used for the epitaxial films; the amorphous film was measured by a 2-wire method because of its high resistance. The sample temperature was controlled by a T95 system controller supplemented with a liquid nitrogen cooling pump LNP 95. Samples were placed inside a HFS600E-PB4 temperature-controlled probe system (all devices are manufactured by Linkam Scientific Instruments Ltd., Tadworth, UK) with a transparent quartz window and 4 tungsten gold-plated tip probes ensuring ohmic contacts.

Commercial laser diodes in a TO-56 CAN package were mounted inside the standard focusing optical modules of Ø12 mm, which were integrated with a fan cooler. The emitted optical power was controlled by a constantly applied current and calibrated by an optical power meter PM100D equipped with a photodiode sensor S121C (Thorlabs Inc, Newton, MA, USA). Four different high-power laser diodes were used: a blue laser (OSRAM PLPT5 447KA) with a 447 nm wavelength and a maximal optical power 1.2 W; a green laser (OSRAM PLT5 520B) with 520 nm, up to 85 mW; a red laser (Panasonic LNCQ28PS01WW) with 660 nm, up to 0.1 W; and an infra-red laser (ADL-80V01NL) with 808 nm, up to 0.4 W. A central uncovered part of the films $3.2 \times 2\text{ mm}^2$ between two inner golden contacts was irradiated. Optical absorption of the film-substrate stacks was also estimated using the same power meter putting the central part of the films between the laser beam and the photodiode sensor S121C. For each laser and film, 3–4 different levels of the optical power

were adjusted to estimate the mean absorption factor with a maximal standard error of the averaging of 2%.

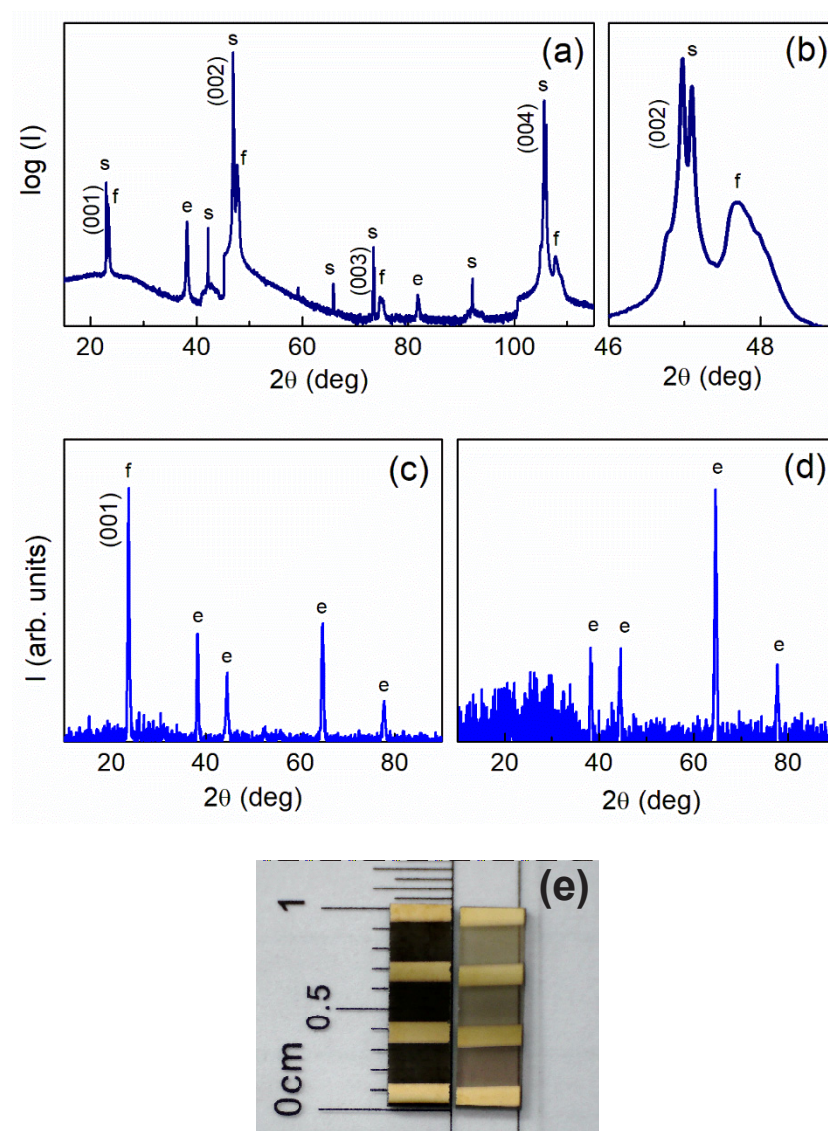


Figure 1. X-ray diffraction analysis of the studied films: (a,b) Bragg–Brentano θ – 2θ scans and (c,d) grazing incidence scans of the NNO films on (a–c) LSAT and (d) SiO_2 substrates. Diffraction peaks from the films, the LSAT substrate and the Au electrodes are marked by f, s, and e, correspondingly. Details of the (002) peaks are shown in (b). (e) Photo of the films: the darker epitaxial film on LSAT is on the left side.

3. Results

Different substrates enabled either epitaxial film growth or the creation of amorphous structure. Epitaxial NNO films that we created on LSAT substrate (clear X-ray diffraction peaks from the film and the substrate are shown in Figure 1a–c), and amorphous NNO films were grown on SiO_2 (the absence of the corresponding peaks is shown in Figure 1d).

Figure 2 presents the resistivity as a function of temperature for both films. As illustrated by Figure 2a, the epitaxial NNO film demonstrates a typical behavior with a pronounced MIT at $T_{MI} \approx -105^\circ\text{C}$ (170 K), a narrow low-temperature hysteresis $\sim 5^\circ\text{C}$ and relevant resistivity values $\rho \approx 0.6\text{ m}\Omega\cdot\text{cm}$ at room temperature [3–9]. Contrary to that, the amorphous film shows a strong insulating behavior with a fivefold exponential drop of resistivity with a temperature increase from 26 to 70°C (see Figure 2b). This dependence

can be fitted with a good accuracy (Pearson correlation coefficient is 0.9998) using an adiabatic polaron hopping model $\sigma T \propto \exp(-E_h/kT)$ [18]. The corresponding linear fit shown in Figure 2c gives a hopping activation energy $E_h \approx 350$ meV.

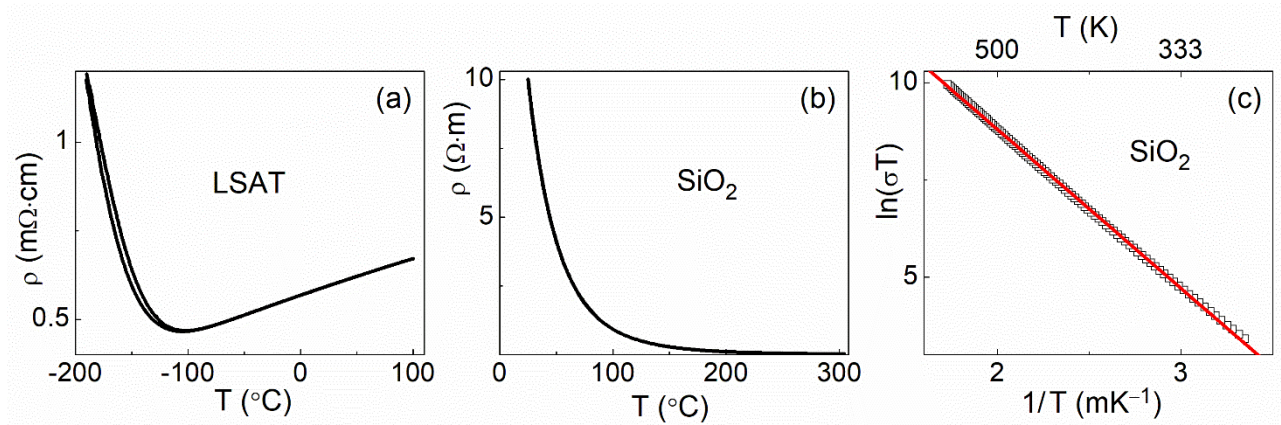


Figure 2. Resistivity temperature dependence at cooling–heating loop for NNO films on (a) LSAT and (b) SiO₂ substrates. (c) Adiabatic polaron hopping fit for the latter dependence.

Figure 3 illustrates the impact of the light irradiation on the resistive properties of both NNO films. Few-second illumination results in a stepwise change of the films resistivity. During 3–5 s of irradiation, the resistivity becomes stable with time if the opposite side of the substrate is held at 26 °C by the temperature controller (see Figures 4a and A1a). For quantitative assessment of the observed photoresistive effect, illumination by the blue laser with 0.8-W optical power is taken as a reference. Such illumination of the central films region for three seconds providing $\sim 0.4 \text{ J}\cdot\text{mm}^{-2}$ energy density leads to a 7.7% increase and 55% decrease in the electrical resistivity for the epitaxial and the amorphous film, respectively. With active temperature controller, the repeatable laser switching leads to reversible changes in the resistivity. If the controller does not operate, additional continuous change in the resistivity and rise in the inbuilt thermocouple reading are observed (see Figures 4b and A1b). Five 15-s pulses of 1.2 W power increase the temperature of a massive silver-coated stage (ceramic disk of 2 cm diameter and 1 cm thickness) by almost 10 °C. The stage temperature increases continuously during each light pulse and decreases much slower between the pulses. At continuous lighting, the resistivity change saturates after ~ 1000 s together with stabilization of the stage temperature on a level >40 °C.

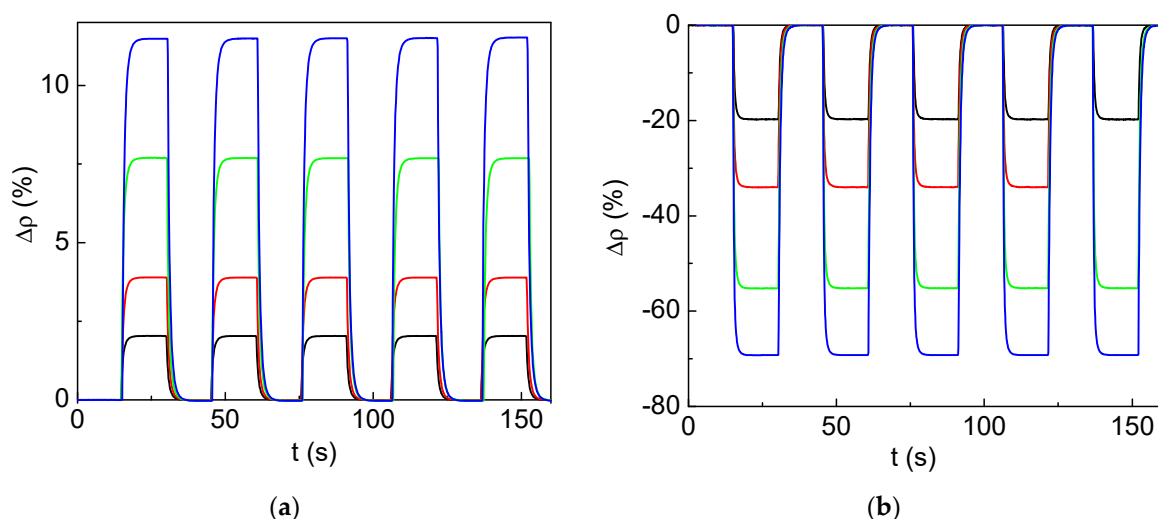


Figure 3. Percentage change of the resistivity for NNO films on (a) LSAT and (b) SiO₂ substrates at fixed temperature $T = 26$ °C and periodical 15-s illumination by the blue laser at different optical power: 0.2, 0.4, 0.8 and 1.2 W.

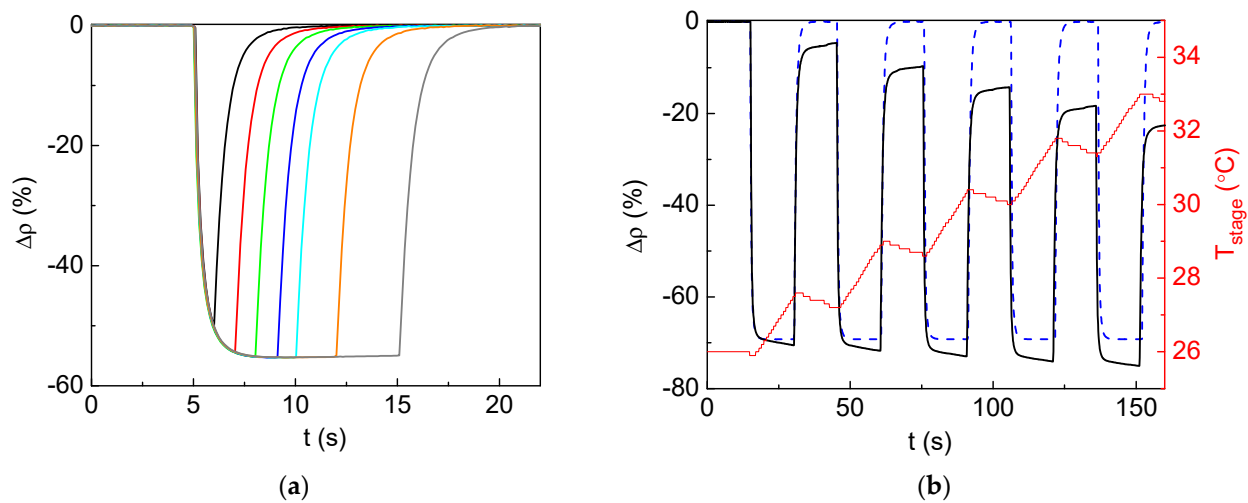


Figure 4. Percentage change of the resistivity at lighting by the blue laser on the amorphous NNO film. (a) Optical power is set to 0.8 W, whereas the durations of the light pulse are varied as 1, 2, 3, 4, 5, 7 and 10 s. (b) Optical power is set to 1.2 W, whereas the temperature controller holds the temperature at 26 °C or does not operate. The reversible resistivity changes at the active controller are shown by blue dashed line. In the latter case, an additional decrease in the resistivity shown by black line is accompanied by heating of the sample stage (reading of the inbuilt thermo couple is shown by red line and referred to the right ordinate axis).

A small positive photoresistive response, similar to that presented in Figure 3a, was obtained for other epitaxial NNO and LNO films in the room-temperature metallic phase (see Figures A2 and A3). Epitaxial films of SNO with similar decaying dependences $\rho(T)$ but smaller resistivity values at room temperature than the amorphous NNO film display a negative photoresistive drop, whose amplitude under the reference blue illumination of $\sim 0.4 \text{ J}\cdot\text{mm}^{-2}$ is $\sim 20\%$ (see Figure A4 and Table A1).

For the epitaxial NNO film, a nearly linear increase in the resistivity with optical power of the incident light is well correlated with its temperature dependence (see Figure 5a). For the amorphous film, a decrease in the photoresistivity with optical power also follows the corresponding $\rho(T)$ dependence, as illustrated by Figure 5b (values of the film resistance R are indicated on the right ordinate axis). Therefore, the magnitude of the resistivity drop is not simply proportional to the incident optical power as for the epitaxial film but is an exponential function of the power. Evidently, different resistivity temperature dependences shown in Figure 2 are responsible for significant distinctions of the photoresistive response in the studied films. The photoresistive effect in the case of illumination with other light wavelengths is qualitatively the same to that obtained with the blue laser (compare Figures 3 and A5). Quantitative difference is discussed in the next section.

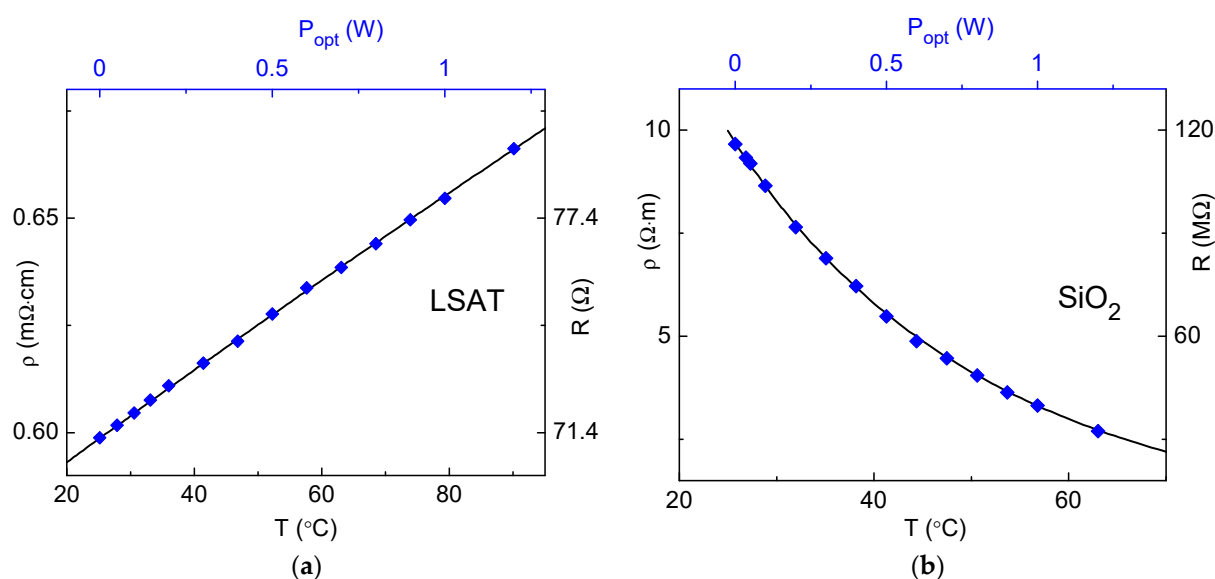


Figure 5. Change of the resistivity with optical power of the blue laser superimposed on the corresponding temperature dependence for NNO films on (a) LSAT and (b) SiO₂ substrates. The right ordinate axes indicate the corresponding resistance values. The temperature controller holds $T = 26^{\circ}\text{C}$.

4. Discussion

Assuming the local film heating is the main reason of the observed photoresistive effect, the appropriate temperature increments can be estimated from the corresponding $\rho(T)$ dependences shown in Figure 5. As illustrated by Figures 6 and A6, such estimated increments ΔT are proportional to the optical power P_{opt} , which gives a constant effective heat capacity of the film-substrate stack. However, the slopes k of the presented linear fits $\Delta T(P_{opt})$ with the Pearson correlation coefficients > 0.9996 are varied with the films and the light wavelengths. These distinctions in the heating ability are mostly ascribed to the different optical absorptions of the films because both substrates are transparent and no significant reflection from the film surface is observed (see Table 1). Even visually, the epitaxial film is much darker than the amorphous one, proving a twice as high absorption factor (see Figure 1e and Ref. [14]). Both film-substrate stacks absorb the light of lower wavelengths better; however, this dependence is not so pronounced for the epitaxial films. Normalization of the fit slopes k by the absorption factor α reduces the parameter variation for the 8 considered cases: total mean values $\langle k \rangle = 37.3 \pm 15.9$ ($\pm 43\%$) but $\langle k/\alpha \rangle = 58 \pm 3.7$ ($\pm 6.4\%$). The latter standard deviation $\sim 6\%$ can be assigned to the light reflection at the film surface and the film-substrate interface (estimated on a level of $\sim 7\%$) as well as to wavelength-dependent light absorption of the LSAT substrate [19,20]. Absorption factor of the commercial crystal quartz is known to be about 10% within a broad wavelength range from ultraviolet to far infrared light. The obtained value $\langle k/\alpha \rangle = 58^{\circ}\text{C}/\text{W}$ is physically reasonable: the energy of 3 J fully absorbed during the 3-s illumination with 1-W optical power could heat the thermally isolated substrates of LSAT and quartz by 49 and 96 $^{\circ}\text{C}$, respectively.

The magnitude of the negative photoresistivity in the amorphous film can be increased by preparing thicker films for higher optical absorption, as well as tuned by a proper manufacturing of the sensitive film structure to optimize its resistance value. Thermal isolation of the film can also tune the photoresistive changes. Improving the substrate-stage contact by thermally conductive grease decreases the time of the resistivity switch up to one second (compare Figures 4a and 7a). However, the magnitude of the photoresistive change also decreases twice. Contrariwise, putting a sheet of paper between the substrate and the temperature-controlled stage increases the magnitude of the photoresistive change as well as the switching time twice (see Figure 7b).

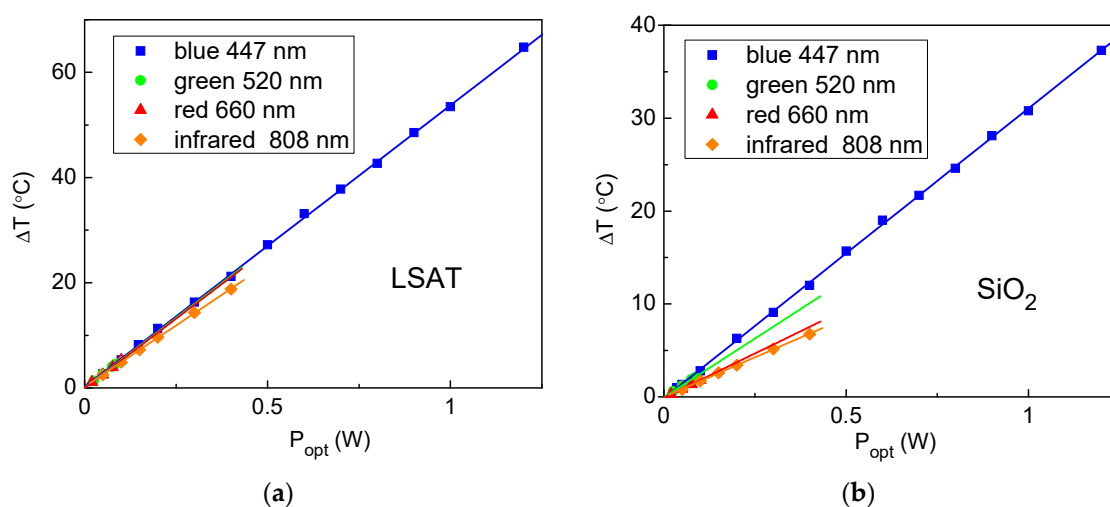


Figure 6. Estimated temperature increments as functions of the optical power for all light wavelengths with the corresponding linear fits for NNO films on (a) LSAT and (b) SiO₂ substrates.

Table 1. The slope k of the linear fits $\Delta T(P_{opt})$ shown in Figure 6, the measured absorption factor α of the film-substrate stack and the ratio k/α for both NNO films and all light wavelengths λ . The absorption factor of the bare LSAT substrate α_s is shown in the fifth column.

λ , nm	LSAT				SiO ₂		
	k , °C/W	α , %	k/α , °C/W	α_s , %	k , °C/W	α , %	k/α , °C/W
447	53.5	91.8	58.3	33.6	31.2	52.8	59.1
520	53.1	88.2	60.3	26.9	25.3	41.7	60.8
660	52.8	83.8	63	24.5	19.1	36.9	51.7
808	46.6	82.8	56.3	8.8	17.1	31.2	54.6

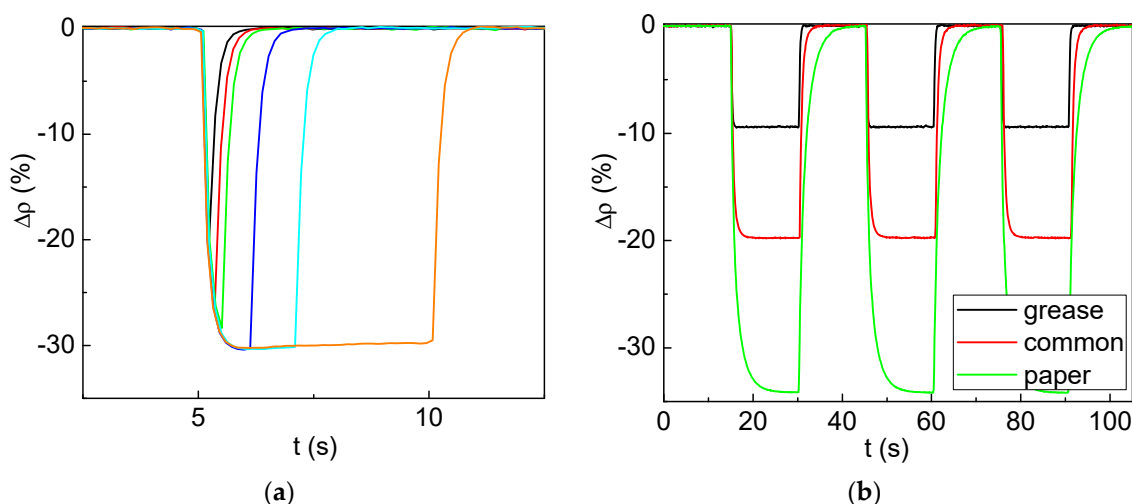


Figure 7. The percentage change of the resistivity at lighting by the blue laser on the amorphous NNO film, whose thermal contact to the temperature-controlled stage ($T = 26$ °C) is varied. (a) Optical power is set to 0.8 W and the substrate-stage contact is improved by thermally conductive grease. Durations of the light pulse are varied as 0.1, 0.25, 0.5, 1, 2 and 5 s. (b) Optical power is set to 0.2 W, whereas the thermal contact between the substrate back-side and the temperature-controlled stage is varied as follows: (i) improved by thermally conductive grease; (ii) leave in the common condition of a freely lying sample; and (iii) a paper sheet of 0.1 mm thickness is placed between the substrate and the cooling stage.

The achievable magnitudes of the photoresistive effect in the amorphous NNO film can be attractive for using in thermal photodetectors [21]. This type of the light detector utilizes the considered principle: it measures temperature rises resulting from the light absorption. The thermal detectors are applied when photon semiconducting detectors are ineffective, in particular, for measuring the long-wavelength infrared light and the high-power lasers. Usually, a black coating covers the temperature sensor for homogeneous broadband absorption. The thermal detectors expectedly suffer from their temperature sensitivity; therefore, an air/water cooling is frequently used. Another strategy is to modulate the incident light with a chopper and to estimate a dark-light relative difference. Typical response time of the thermal detectors is a few seconds. Sensitivity of such industrial sensors is not declared by the producers. However, the observed huge photoresistance change $\sim 527 \text{ M}\Omega/\text{W}\cdot\text{mm}^{-2}$ with the similar time response at the reference 0.8 W blue light illumination should be competitive (see Figure 5b).

The competitive analysis can be performed estimating an amorphous film potential for industrial temperature sensing since the same physical principle is in play; the exponential decay of the resistivity with heating is illustrated by Figures 2b and 5b. Such a dependence is typical for thermistors with negative temperature coefficient, i.e., thermally sensitive resistors with negative dR/dT , which are generally made of ceramics or polymers. An important figure of merit for the thermometer layer material is the temperature coefficient of resistance $\alpha = (dR/dT)/R$, whose typical values range from -3 to $-6\% \text{ } ^\circ\text{C}^{-1}$ [22]. Another important characteristic of the thermistors is a so-called B value defined by Equation (1) (both temperatures are in Kelvin):

$$B_{T1/T2} = \frac{T_2 \cdot T_1}{T_2 - T_1} \cdot \ln\left(\frac{R_1}{R_2}\right) \quad (1)$$

Typical $B_{25/100}$ values for the thermistors with negative temperature coefficient are between ~ 3000 and 5000 K . As illustrated by Figure 8, values of these parameters estimated for the presented amorphous film are industrially competitive. This is especially true for the range of rapid resistivity decay $T = 25\text{--}75 \text{ } ^\circ\text{C}$, which is an operation range of semiconductor electronics. Therefore, a thin film element of the amorphous NNO can be effective as a microchip-inbuilt temperature sensor. The range of the highest R changes can be optimized varying the NNO film thickness/length. Moreover, amorphous SNO films are expected to provide similar resistivity decay at much higher temperatures, which could be also industrially attractive. The thermistors are typically suitable for use within a temperature range between -55 and $200 \text{ } ^\circ\text{C}$. For the higher temperatures in the order of $600 \text{ } ^\circ\text{C}$, thermocouples are usually used instead of the thermistors.

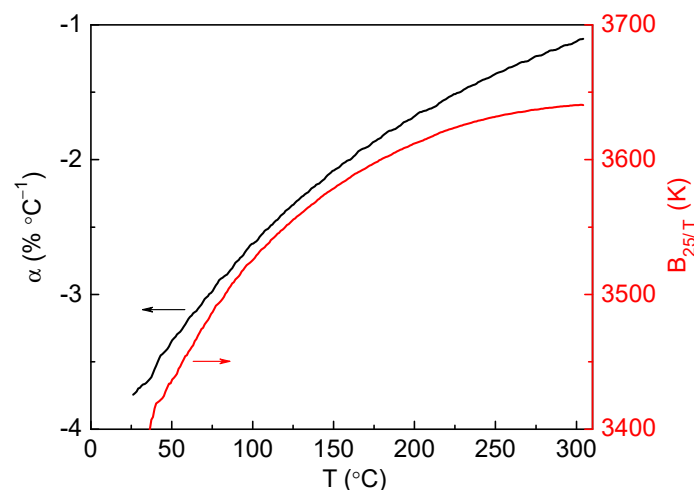


Figure 8. Temperature coefficient of resistance α and B_{25} value (black/red lines referred to the left/right axes, respectively) as functions of temperature for the amorphous NNO film.

5. Conclusions

The novel material, amorphous film of NdNiO₃, demonstrates useful resistive properties at room temperature: measurable resistance $\sim 110 \text{ M}\Omega$, which exponentially drops with increasing temperature (temperature coefficient of resistance is about $-3\% \text{ } ^\circ\text{C}^{-1}$). This opens a promising opportunity for developing sensitive microelectronic temperature sensors (thermistors). A large negative photoresistivity ($\sim 55\%$ under blue lighting with $\sim 0.4 \text{ J}\cdot\text{mm}^{-2}$ energy density) is additionally observed in the amorphous NdNiO₃ film, which make it an attractive material for thermal photodetectors. Contrary to the epitaxial films deposited on expensive high-quality perovskite substrates, the amorphous films can be deposited on any industrially attractive substrates such as glass, quartz or silicon, which provides a serious technical advantage. The presented results evidence that a local film heating plays an important role in the observed photoresistive response. Any noticeable excitation of the electronic states by visible and infra-red light was not observed for the studied epitaxial and amorphous NdNiO₃ films in the room temperature range. This important outcome should prevent further speculations in the field of nickelate research and indicate challenging directions for further development of these perovskite materials.

Author Contributions: Conceptualization, M.T. and A.S.; methodology, T.K., N.N. and A.S.; software, A.S.; validation, A.S., M.T. and A.D.; formal analysis, A.S., N.N. and M.T.; investigation, A.S.; resources, A.D.; writing—original draft preparation, A.S.; writing—review and editing, M.T. and A.D.; visualization, A.S.; supervision, M.T. and A.D.; project administration, A.S. All authors have read and agreed to the published version of the manuscript.

Funding: This research was funded by the Czech Science Foundation (GA ĆR), grant number 20-21864S.

Institutional Review Board Statement: Not applicable.

Informed Consent Statement: Not applicable.

Data Availability Statement: The data that support the findings of this study are available from the corresponding author upon reasonable request.

Conflicts of Interest: The authors declare no conflict of interest.

Appendix A

Figures A2a and A3a present the resistivity as a function of temperature for other tested epitaxial films of NNO and LNO deposited on LSAT or LAO. All these films have metallic resistive behavior at room temperature. Only another NNO film on LSAT of 20 nm thickness demonstrates a similar MIT behavior as the reference epitaxial film considered in the main text (compare Figures 2a and A2a). The rest of the tested films do not display MIT above $-190 \text{ } ^\circ\text{C}$, which is common for these materials and substrates [6–9]. Blue light illumination with the reference optical power 0.8 W ($\sim 0.4 \text{ J}\cdot\text{mm}^{-2}$ energy density) results in a comparable increase in the film resistivity by 5–8% (compare Figures 3a, A2b and A3b). Figure A4a presents the resistivity as a function of temperature for tested epitaxial films of SNO deposited on LSAT or LAO. All SNO films demonstrate insulating behavior at room temperature with a lower resistivity drop and increasing temperature as compared to the amorphous NNO film (compare with Figure 2b). This results in a lower photoresistivity drop $\sim 20\%$, as illustrated by Figure A4b. Table A1 compares the magnitude of the observed photoresistive effect for all tested films at room temperature under the reference blue light illumination with $\sim 0.4 \text{ J}\cdot\text{mm}^{-2}$ energy density.

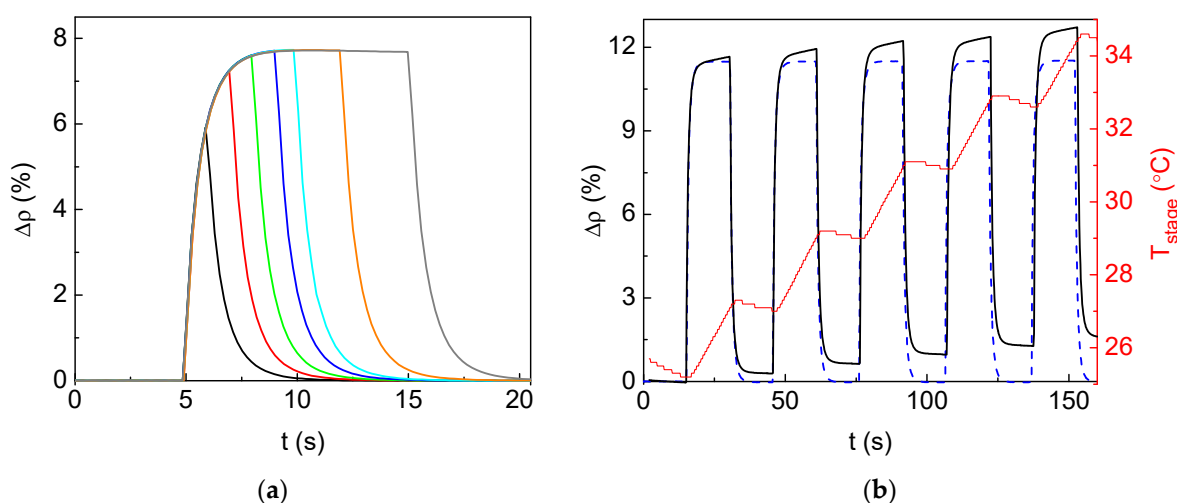


Figure A1. Percentage change of the resistivity at lighting by the blue laser on the epitaxial NNO film. (a) Optical power is set to 0.8 W, whereas the durations of the light pulse are varied as 1, 2, 3, 4, 5, 7 and 10 s. (b) Optical power is set to 1.2 W, whereas the temperature controller holds the temperature at 26 $^{\circ}\text{C}$ or does not operate. The reversible resistivity changes at the active controller are shown by blue dashed line. In the latter case, an additional increase in the resistivity shown by black line is accompanied by heating of the sample stage (reading of the inbuilt thermocouple is shown by red line and referred to the right ordinate axis).

It is worth noting that the data presented in Figures A2b and A3b were obtained in a simpler mode than those in Figure 3. Here the illumination was applied by supplying a constant current to the laser diode. The disadvantage of this simple method is that the diode is heated by $\sim 5\text{--}7\text{ }^{\circ}\text{C}$ during the first few minutes after the current supply, which is accompanied by a loss in the emitted optical power. This causes small initial leaps in the photoresistive profiles. During ~ 100 s, the laser temperature stabilizes together with the emitted power, which was checked by the optical power meter. Additional experiments were performed where the stabilized laser beam is chopped mechanically (dashed profiles in Figures A2b and A3b). The photoresistive changes obtained at periodical 15-s illumination, including all data presented in the main text, were measured using the stabilized laser, whose beam was chopped by a half-disk shutter attached to a stepping motor.

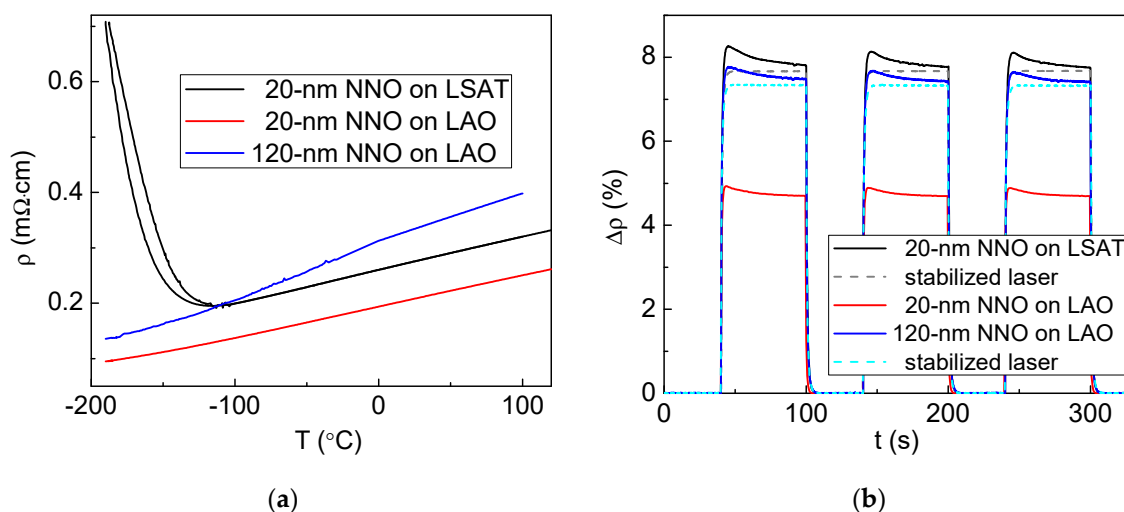


Figure A2. (a) Resistivity temperature dependence for other tested NNO films: two 20-nm thick films deposited on LSAT and LAO and a 120-nm thick film on LAO. (b) Percentage change of their room-temperature resistivity at periodical 60-s illumination by the blue laser at optical power 0.8 W.

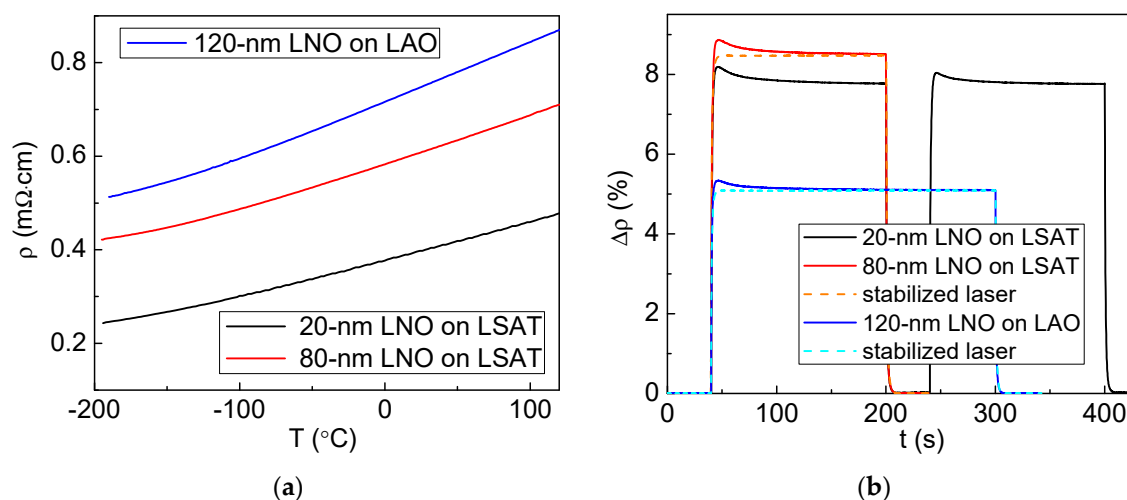


Figure A3. (a) Resistivity temperature dependence for other tested LNO films: two films deposited on LSAT with thicknesses 20 and 80 nm as well as a 120-nm thick film on LAO. (b) Percentage change of their room-temperature resistivity at long-term illuminations by the blue laser at optical power 0.8 W.

By analyzing Table A1 in general, it is evident that the magnitude of the photoresistive change can be tuned by a proper manufacturing of the sensitive film structure with defined values of the resistivity and its derivative $d\rho/dT$. However, the thermal factors, namely optical absorption and heat removal, prevail. The absorption factor of the dark perovskite films is high: ~80% for the thin 20-nm films and >90% for the thicker films (see Figure 1e). This determines a higher heating of the thicker films. A lower heating of the films on LAO is caused by its twice bigger thermal conductivity $10 \text{ W/m}\cdot\text{K}$ as compared to that of LSAT: $5.1 \text{ W/m}\cdot\text{K}$. It is also proved by smaller slopes k of the linear fits $\Delta T(P_{\text{opt}})$ in Figure A6: 21.7 and $27.6 \text{ }^{\circ}\text{C/W}$, respectively, for the blue light (20.1 and $24.1 \text{ }^{\circ}\text{C/W}$ for the infra-red illumination). The corresponding ratios k/α are 28.2 and $32.1 \text{ }^{\circ}\text{C/W}$, which is very close to a half of that value obtained for the NNO film on LSAT (see Table 1).

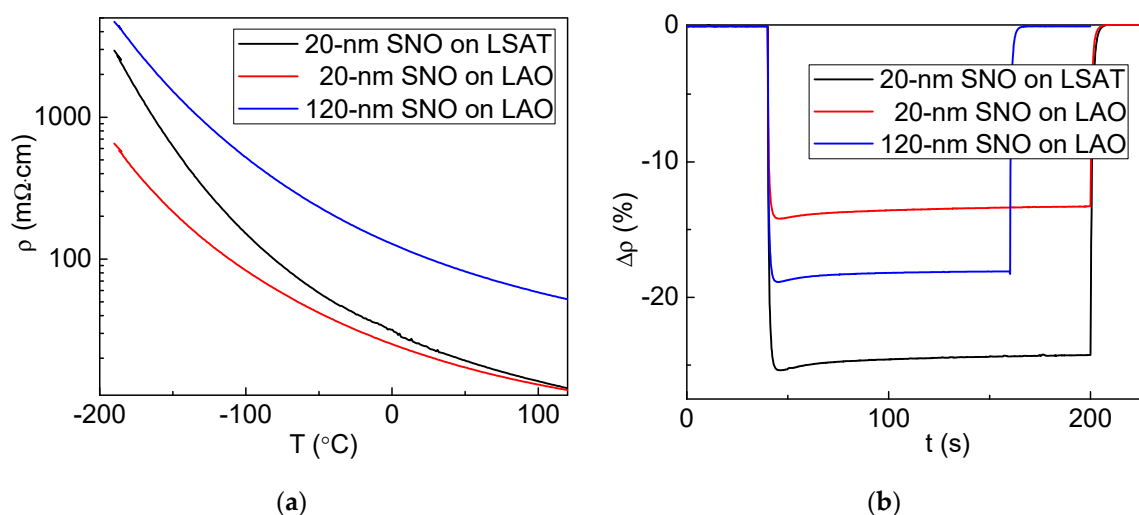


Figure A4. (a) Resistivity temperature dependence for other tested SNO films: two 20-nm thick films deposited on LSAT and LAO and a 120-nm thick film on LAO. (b) Percentage change of their room-temperature resistivity at long-term illuminations by the blue laser at optical power 0.8 W.

Table A1. Photoresistivity parameters for all tested films at $T = 26\text{ }^{\circ}\text{C}$ and the reference blue light illumination of 0.8 W power: percentage changes of the resistivity $\Delta\rho$, the measured absorption factors α of the film-substrate stacks, resistivity values ρ , derivatives $d\rho/dT$ and estimated rises of the film temperature ΔT .

Film	NNO					LNO			SNO		
Substrate	LSAT		LAO		SiO ₂	LSAT		LAO	LSAT	LAO	
Thickness, nm	20	80	20	120	80	20	80	120	20	20	120
$\Delta\rho$, %	7.7	7.7	4.7	7.4	−55	7.8	8.5	5.1	−24	−13.4	−18
α , %	83.7	91.8	77.2	96.5	52.8	79.8	92	96.2	80.3	71.9	86
ρ , m $\Omega\cdot\text{cm}$	0.277	0.6	0.21	0.34	10^6	0.4	0.61	0.76	25.2	22.3	99.5
$d\rho/dT$, $\mu\Omega\cdot\text{cm}/\text{K}$	0.61	1.1	0.57	0.88	$-36\cdot 10^6$	0.88	1	1.3	−231	−172	−731
ΔT , $^{\circ}\text{C}$	36	42.7	17	29	25	35	50	30	35	20	25

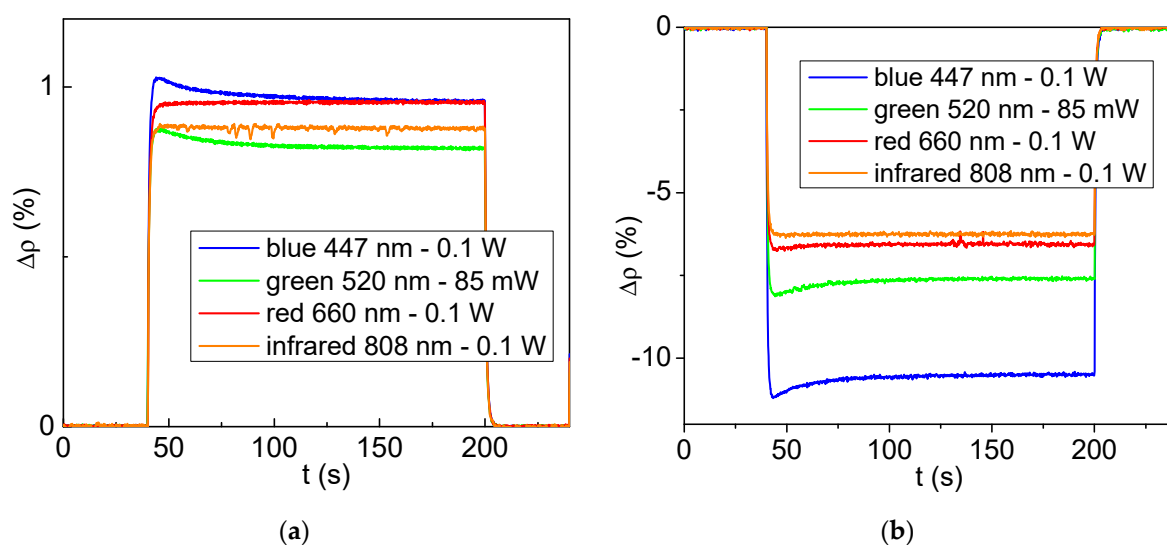


Figure A5. Percentage change of the resistivity for NNO films on (a) LSAT and (b) SiO₂ substrates at fixed temperature $T = 26\text{ }^{\circ}\text{C}$ and long-term illumination by different lasers at optical power 0.1 W (except the green laser, which maximal power is 85 mW).

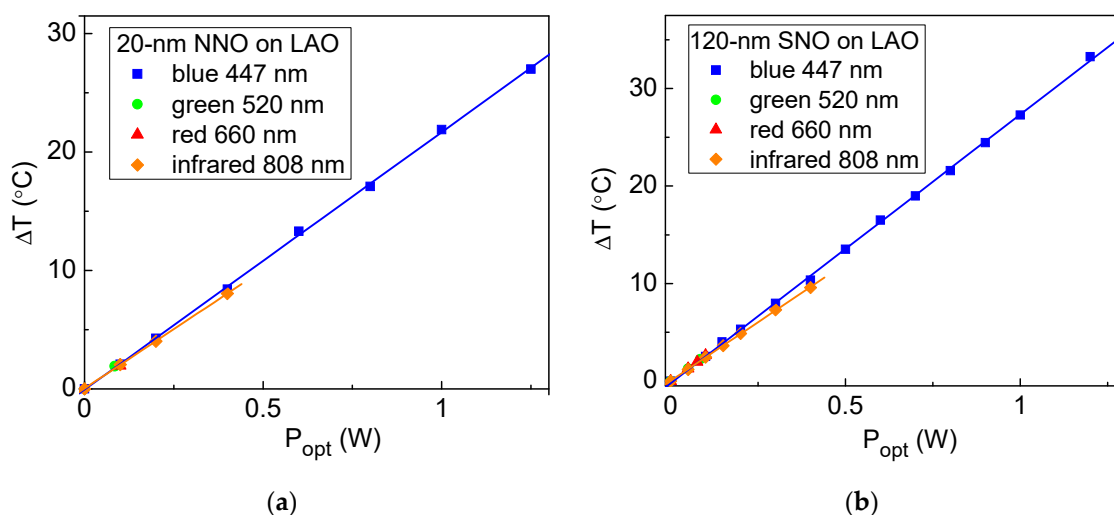


Figure A6. Estimated temperature increments as functions of the optical power for all light wavelengths with the corresponding linear fits for (a) the 20-nm thick NNO and (b) the 120-nm thick SNO films on LAO.

Table values of the heat capacity and the density (0.57 and 0.733 J/g·K as well as 6.74 and 2.65 g/cm³ for LSAT and quartz, respectively) are taken to estimate a heating of the isolated substrates of 3.2 × 10 mm size in the main text.

References

1. Park, J.; Lim, Y.; Kong, S.; Lee, H.; Kim, Y.-B. Rapid fabrication of chemical solution-deposited lanthanum nickelate thin films via intense pulsed-light process. *Coatings* **2019**, *9*, 372. [\[CrossRef\]](#)
2. Medarde, M.L. Structural, magnetic and electronic properties of RNiO₃ perovskites (R = rare earth). *J. Phys. Condens. Matter*. **1997**, *9*, 1679–1707. [\[CrossRef\]](#)
3. Catalan, G. Progress in perovskite nickelate research. *Phase Transit.* **2008**, *81*, 729–749. [\[CrossRef\]](#)
4. Middey, S.; Chakhalian, J.; Mahadevan, P.; Freeland, J.W.; Millis, A.J.; Sarma, D.D. Physics of ultrathin films and heterostructures of rare-earth nickelates. *Annu. Rev. Mater. Res.* **2016**, *46*, 305–334. [\[CrossRef\]](#)
5. Catalano, S.; Gibert, M.; Fowlie, J.; Íñiguez, J.; Triscone, J.-M.; Kreisel, J. Rare-earth nickelates RNiO₃: Thin films and heterostructures. *Rep. Prog. Phys.* **2018**, *81*, 046501. [\[CrossRef\]](#) [\[PubMed\]](#)
6. Liu, J.; Kargarian, M.; Kareev, M.; Gray, B.; Ryan, P.J.; Cruz, A.; Tahir, N.; Chuang, Y.D.; Guo, J.; Rondinelli, J.M.; et al. Heterointerface engineered electronic and magnetic phases of NdNiO₃ thin films. *Nat. Commun.* **2013**, *4*, 2714. [\[CrossRef\]](#) [\[PubMed\]](#)
7. Wang, L.; Ju, S.; You, L.; Qi, Y.; Guo, Y.; Ren, P.; Zhou, Y.; Wang, J. Competition between strain and dimensionality effects on the electronic phase transitions in NdNiO₃ films. *Sci. Rep.* **2015**, *5*, 18707. [\[CrossRef\]](#) [\[PubMed\]](#)
8. Mikheev, E.; Hauser, A.J.; Himmetoglu, B.; Moreno, N.E.; Janotti, A.; Van de Walle, C.G.; Stemmer, S. Tuning bad metal and non-Fermi liquid behavior in a Mott material: Rare-earth nickelate thin films. *Sci. Adv.* **2015**, *1*, e1500797. [\[CrossRef\]](#) [\[PubMed\]](#)
9. Stupakov, A.; Pacheroova, O.; Kocourek, T.; Jelinek, M.; Dejneka, A.; Tyunina, M. Negative magnetoresistance in epitaxial films of neodymium nickelate. *Phys. Rev. B* **2019**, *99*, 085111. [\[CrossRef\]](#)
10. Liao, Z.; Gauquelin, N.; Green, R.J.; Müller-Caspary, K.; Lobato, I.; Li, L.; Van Aert, S.; Verbeeck, J.; Huijben, M.; Grisolia, M.N.; et al. Metal–insulator–transition engineering by modulation tilt-control in perovskite nickelates for room temperature optical switching. *Proc. Natl. Acad. Sci. USA* **2018**, *115*, 9515–9520. [\[CrossRef\]](#)
11. Ahn, C.; Cavalleri, A.; Georges, A.; Ismail-Beigi, C.; Millis, A.J.; Triscone, J.-M. Designing and controlling the properties of transition metal oxide quantum materials. *Nat. Mater.* **2021**, *20*, 1462–1468. [\[CrossRef\]](#)
12. Mattoni, G.; Manca, N.; Hadjimichael, M.; Zubko, P.; van der Torren, A.J.; Yin, C.; Catalano, S.; Gibert, M.; Maccherozzi, F.; Liu, Y.; et al. Light control of the nanoscale phase separation in heteroepitaxial nickelates. *Phys. Rev. Mater.* **2018**, *2*, 085002. [\[CrossRef\]](#)
13. Chen, B.; Gauquelin, N.; Jannis, D.; Cunha, D.M.; Halisdemir, U.; Piamonteze, C.; Lee, J.H.; Belhadi, J.; Eltes, F.; Abel, S.; et al. Strain-engineered metal-to-insulator transition and orbital polarization in nickelate superlattices integrated on silicon. *Adv. Mater.* **2020**, *32*, 2004995. [\[CrossRef\]](#)
14. Sun, Y.; Wang, Q.; Park, T.J.; Gage, T.E.; Zhang, Z.; Wang, X.; Zhang, D.; Sun, X.; He, J.; Zhou, H.; et al. Electrochromic properties of perovskite NdNiO₃ thin films for smart windows. *ACS Appl. Electron. Mater.* **2021**, *3*, 1719–1731. [\[CrossRef\]](#)
15. Lin, T.-K.; Chang, H.-W.; Chou, W.-C.; Wang, C.-R.; Wei, D.-H.; Tu, C.-S.; Chen, P.-Y. Multiferroic and nanomechanical properties of Bi_{1-x}Gd_xFeO₃ polycrystalline films (x = 0.00–0.15). *Coatings* **2021**, *11*, 900. [\[CrossRef\]](#)
16. Thiruchelvan, P.S.; Lai, C.-C.; Tsai, C.-H. Combustion processed nickel oxide and zinc doped nickel oxide thin films as a hole transport layer for perovskite solar cells. *Coatings* **2021**, *11*, 627. [\[CrossRef\]](#)
17. Simandan, I.-D.; Sava, F.; Buruiana, A.-T.; Burducea, I.; Becherescu, N.; Mihai, C.; Velea, A.; Galca, A.-C. The effect of the deposition method on the structural and optical properties of ZnS thin films. *Coatings* **2021**, *11*, 1064. [\[CrossRef\]](#)
18. Thiessen, A.; Beyreuther, E.; Werner, R.; Koelle, D.; Kleiner, R.; Eng, L.M. Quantifying the electrical transport characteristics of electron-doped La_{0.7}Ce_{0.3}MnO₃ thin films through hopping energies, Mn valence, and carrier localization length. *J. Phys. Chem. Solids* **2015**, *80*, 26–33. [\[CrossRef\]](#)
19. Nunley, T.N.; Willett-Gies, T.I.; Cooke, J.A.; Manciu, F.S.; Marsik, P.; Bernhard, C.; Zollner, S. Optical constants, band gap, and infrared-active phonons of (LaAlO₃)_{0.3}(Sr₂AlTaO₆)_{0.35} (LSAT) from spectroscopic ellipsometry. *J. Vac. Sci. Technol. A* **2016**, *34*, 051507. [\[CrossRef\]](#)
20. Müllerová, J.; Šutta, P.; Holá, M. Optical absorption in Si:H thin films: Revisiting the role of the refractive index and the absorption coefficient. *Coatings* **2021**, *11*, 1081. [\[CrossRef\]](#)
21. Voshell, A.; Terrones, M.; Rana, M. Thermal and photo sensing capabilities of mono- and few-layer thick transition metal dichalcogenides. *Micromachines* **2020**, *11*, 693. [\[CrossRef\]](#) [\[PubMed\]](#)
22. Le, D.T.; Ju, H. Solution synthesis of cubic spinel Mn–Ni–Cu–O thermistor powder. *Materials* **2021**, *14*, 1389. [\[CrossRef\]](#) [\[PubMed\]](#)